MATERIALS SCIENCE

Intracellular action potential recordings from cardiomyocytes by ultrafast pulsed laser irradiation of fuzzy graphene microelectrodes

Michele Dipalo[1†], Sahil K. Rastogi[2†], Laura Matino[3,4], Raghav Garg[5], Jacqueline Bliley[2], Giuseppina Iachetta[1], Giovanni Melle[1], Ramesh Shrestha[6], Sheng Shen[6], Francesca Santoro[3], Adam W. Feinberg[2,5], Andrea Barbaglia[1], Tzahi Cohen-Karni[2,5]*, Francesco De Angelis[1]*

Graphene with its unique electrical properties is a promising candidate for carbon-based biosensors such as microelectrodes and field effect transistors. Recently, graphene biosensors were successfully used for extracellular recording of action potentials in electrogenic cells; however, intracellular recordings remain beyond their current capabilities because of the lack of an efficient cell poration method. Here, we present a microelectrode platform consisting of out-of-plane grown three-dimensional fuzzy graphene (3DFG) that enables recording of intracellular cardiac action potentials with high signal-to-noise ratio. We exploit the generation of hot carriers by ultrafast pulsed laser for porating the cell membrane and creating an intimate contact between the 3DFG electrodes and the intracellular domain. This approach enables us to detect the effects of drugs on the action potential shape of human-derived cardiomyocytes. The 3DFG electrodes combined with laser poration may be used for all-carbon intracellular microelectrode arrays to allow monitoring of the cellular electrophysiological state.

INTRODUCTION

Monitoring the electrical activity of neurons and cardiomyocytes is of fundamental importance to study the electrophysiology of the brain and the heart, investigate neurodegenerative or cardiac diseases, and develop new therapeutic strategies. Microelectrode array (MEA) platforms have been extensively used because of their ability to monitor large cell ensembles by measuring electrical signals from hundreds/thousands of cells simultaneously (*1*). In particular, in in vitro applications, the MEA approaches provide an ideal balance between accuracy and high throughput because of the recent implementation of novel two-dimensional (2D) and 3D metal electrode configurations (*2*–*4*), which enable the recording of intracellular-like action potentials (APs).

The extraordinary properties of graphene, such as biocompatibility (*5*), high electrical conductivity (*6*), and flexibility (*7*), have made it a great candidate for developing MEAs and transistors to study electrophysiology of excitable cells (*8*–*11*). However, to date, graphene-based devices have been limited to extracellular field potential (FP) recordings, which do not capture the major features of an AP as can be performed with patch clamp (*12*). This limits considerably the applicability of graphene microelectrodes in in vitro electrophysiology because the capability to monitor intracellular APs accurately is an essential requirement in toxicology studies and drug screening assays (*13*, *14*).

Optical generation of energetic carriers (hot carriers) in water using nanomaterials, such as porous Pt, has been shown to porate the cellular membrane in a very localized and noninvasive manner (*15*). In graphene-based materials, optical illumination has been demonstrated to result in the generation of hot carriers (*16*, *17*). Hence, laser stimulation of graphene-based MEAs may lead to local cell membrane poration (optoporation) enabling intracellular recording. Furthermore, increasing the available surface area of graphene-based electrodes is expected to lead to a higher degree of hot carrier generation upon laser illumination, thus lowering the intensity of the laser required to porate the cells. We recently reported a high–surface area graphene-based nanostructure: 3D fuzzy graphene (3DFG) (*18*). The morphology of 3DFG makes it an ideal candidate to enable optoporation of excitable cells for intracellular recording of electrical activity.

Here, we demonstrate intracellular recordings of cardiac APs by optoporation using 3DFG MEAs. The optoporation of the cell membrane is enabled by the generation of hot carriers in the 3DFG electrodes upon illumination with ultrafast pulsed laser in the near-infrared (NIR) regime. The combination of optoporation and the high effective surface area of 3DFG allows the recording of APs with high signal-to-noise ratio (SNR), enabling the identification of the effects of various drugs on the ionic currents in cardiomyocytes. The out-of-plane morphology of graphene flakes further leads to a tight adhesion of the plasma membrane to 3DFG electrodes, as observed through cross-sectional scanning electron microscopy (SEM) imaging of the cardiomyocyte–3DFG electrode interface. This work will enable the development of flexible, low-cost, and biocompatible all-carbon MEA platform for intracellular recordings of electrical activity. Furthermore, the low work function of graphene in the NIR-II window (1000 to 1700 nm) may enable the application of cell poration in thicker tissues and organoids, which are less absorbing and less scattering in the NIR-II window (*19*).

[1]Istituto Italiano di Tecnologia, Genova 16163, Italy. [2]Department of Biomedical Engineering, Carnegie Mellon University, Pittsburgh, PA 15213, USA. [3]Tissue Electronics, Center for Advanced Biomaterials for Healthcare, Istituto Italiano di Tecnologia, Naples 80125, Italy. [4]Dipartimento di Ingegneria Chimica, dei Materiali e delle Produzioni Industriali, DICMAPI, Università 'Federico II', Naples 80125, Italy. [5]Department of Materials Science and Engineering, Carnegie Mellon University, Pittsburgh, PA 15213, USA. [6]Department of Mechanical Engineering, Carnegie Mellon University, Pittsburgh, PA 15213, USA.
*Corresponding author. Email: francesco.deangelis@iit.it (F.D.A.); tzahi@andrew.cmu.edu (T.C.-K.)
†These authors contributed equally to this work.

RESULTS AND DISCUSSION

SEM, optical, and photoelectrical characterization

3DFG was synthesized via plasma-enhanced chemical vapor deposition (PECVD) following previously reported procedures (*18*). Tuning the synthesis parameters, such as synthesis time, allows us to tailor the size and density of out-of-plane graphene flakes (*18*). Functional 3DFG MEAs were fabricated following standard micro- and nanofabrication processes (fig. S1; for details regarding 3DFG fabrication, see Materials and Methods). The out-of-plane morphology of 3DFG is conserved following MEA fabrication procedure and resulted in high–surface area microelectrodes (Fig. 1A and fig. S2; for details regarding structural and electrochemical characterization of 3DFG MEAs, see notes S1 and S2).

Increasing the size and density of the out-of-plane graphene flakes led to an increase in the ultraviolet-visible (UV-Vis) absorbance, as can be seen in the acquired UV-Vis spectra (Fig. 1B). The enhanced absorption can be attributed to increased light trapping by out-of-plane graphene flakes, as the structure is synonymous to that of nanotextured silicon and carbon metamaterials (*20*–*22*). To investigate the type of optical response of 3DFG, we characterized 3DFG films synthesized at 800°C for 90 min on fused silica substrates, with ellipsometry for extracting the real and imaginary parts of the dielectric constant (permittivity) of the material in the visible and NIR range (Fig. 1C). The permittivity provides information on the kind of interaction between the impinging photons and the material. In particular, if the material presents a negative real permittivity and is interfaced with a material with positive real permittivity (e.g., air or water), the impinging photons can strongly interact with it through the excitation of surface plasmon polaritons (*23*).

Our measurements of 3DFG dielectric constants suggest that 3DFG does not present a plasmonic behavior between 300 and 1700 nm, having a positive dielectric constant (ε_1) as presented in Fig. 1C. Consequently, we evaluated the possible photocurrent generated by laser excitation on 3DFG by measuring the hot carriers' extraction from the material in phosphate-buffered saline (PBS). The measurements were performed using a patch-clamp amplifier connected to a 3DFG microelectrode (fig. S3). For excitation, we used a focused picosecond-pulsed laser at 1064 nm, as this represents an optimal configuration for performing cell poration by means of optoacoustic-generated nanoshockwaves (*15*). During excitation, the laser was focused on the 3DFG surface with a spot size of 2 μm in diameter, which resulted in power densities from 414 to 2419 W/mm^2 for the measured average incident power of the laser (1.3 to 7.6 mW, respectively). Figure 1D depicts the photocurrent generated at the interface between 3DFG and PBS during laser stimulation at various intensities. The behavior of the current generated by the 6-ms laser pulse trains suggests a combination of capacitive and faradaic currents, as previously observed for Si-based nanomaterials (*24*). In detail, we observe a pronounced initial current peak at the laser onset followed by a quasi-steady current plateau during the laser pulse train. After the termination of the laser pulse train, a negative current peak with a lower amplitude is observed. Figure 1E reports the

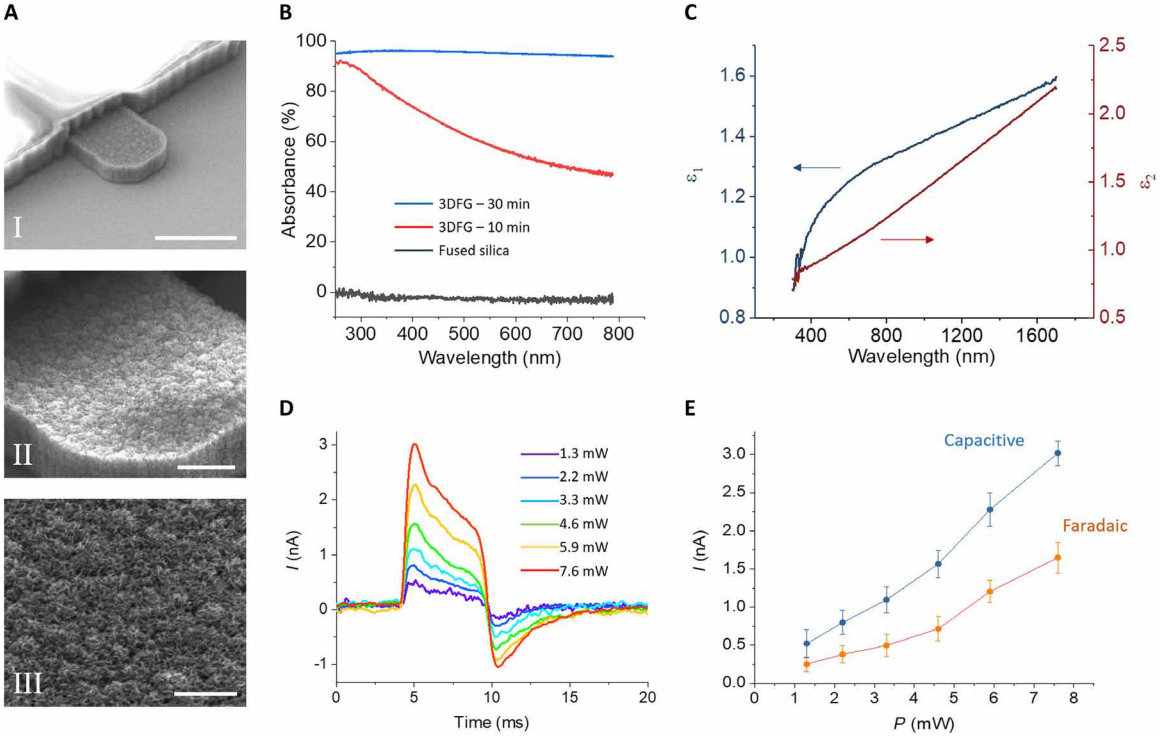

Fig. 1. 3DFG SEM imaging and optical characterization. (**A**) SEM images of 5-μm 3DFG electrodes. Scale bars, 5 μm (I), 1 μm (II), and 0.5 μm (III). (**B**) UV-vis absorbance as a function of wavelength for fused silica (gray), 3DFG synthesized at 800°C for 10 min (red), and 3DFG synthesized at 800°C for 30 min (blue). (**C**) Real (ε_1) and imaginary (ε_2) parts of the dielectric constant of 3DFG in the visible and near-infrared range. (**D**) Photocurrent generated at the interface between 3DFG electrodes and PBS under excitation with ultrafast (picosecond) pulsed laser at 1064 nm at varying laser intensities. The pulse trains have a duration of 6 ms. (**E**) Capacitive and faradaic current components of the photocurrent generated by laser excitation. The capacitive values were taken as the maximum current peak at the onset of the laser excitation. The faradaic values were calculated as the average of the last 1-ms-long portion before the end of the laser pulse train.

capacitive and faradaic currents at the different laser intensities. We suggest that the faradaic current might be related to the emission of hot carriers from 3DFG, high-energy electrons that are out of thermal equilibrium and are expelled by the material and injected into the electrolyte. The generation of hot electron in graphene-based 3D nanostructures has been previously demonstrated (*25*). These generated hot carriers have been proposed to be ejected from graphene following Auger-like mechanism (*25*).

In a previous work, nanowire-templated 3DFG (NT-3DFG) was shown to exhibit high photothermal response under low-power laser illumination (*26*), ascribable to an opto-capacitive rather than faradaic regime (*27*). Although these results suggest dominant photothermal phenomenon in 3DFG, we have identified key distinguishing factors that might be responsible for the observed faradaic response in the current study. The peak power of the laser used during the picosecond-long laser pulse for the photocurrent measurements ranges from 1.5 to 11 W. This range of laser power values are orders of magnitude higher than that reported in the previous work about NT-3DFG (*26*). Furthermore, the spot size of the laser used in this work is smaller than that used in the previous study (2 μm versus 20 μm, respectively) (*26*). For the same incident laser power, the average power density in the current measurements is, therefore, ca. 100 times higher. This suggests that the laser-stimulated emission of hot carriers from 3DFG may follow a threshold mechanism and thus may occur only at high peak power densities, as previously observed in other materials (*28*). However, the exact mechanism describing the generation of hot electrons in 3DFG by ultrafast pulsed laser stimulation will need further exploration.

3DFG MEA–cardiomyocyte interface

Because high biocompatibility is crucial to enable long-term stable interfaces with cells (*29*), we first investigated possible toxic effects of 3DFG by assessing cell viability of human embryonic stem cell–derived cardiomyocytes (hESC-CMs). The viability and stress assays confirm that 3DFG does not induce cell toxicity (note S3 and fig. S4).

Subsequently, to investigate cell growth and health conditions on 3DFG electrodes, human induced pluripotent stem cell–derived cardiomyocytes (hiPSC-CMs) were cultured on 3DFG MEAs and immunohistochemistry fluorescence labeling was performed. On hiPSC-CMs, the results demonstrated a substantial expression of cardiac troponin T (green) that highlights a myocardial structure, as expected for mature hiPSC cardiomyocytes (Fig. 2A) (*30*). The images also show a substantially low expression of NKX2-5 (red), a marker of cardiac progenitor cells, with only 15.38 ± 3.47% of the cells expressing NKX2-5. This confirms the overall correct maturation of the cardiac cell culture (*31*).

We also evaluated the interface between the 3DFG and cardiomyocytes by cross-sectional focused ion beam–SEM imaging. HL-1 cells and hiPSC-CMs were cultured on 3DFG for 24 hours before fixation and dehydration (*32*). The top/tilted-view SEM images of hiPSC-CMs (Fig. 2B) and cross-sectional SEM images of HL-1 cells (Fig. 2C) cultured on 3DFG electrodes confirm tight adhesion between the cell membrane and 3DFG.

Extracellular and intracellular recordings using 3DFG MEA

We cultured hiPSC-CMs on 3DFG MEAs following previously reported protocols (*33*). After a minimum of 3 days in culture, hiPSC-CMs acquire spontaneous and regular electrical activity and mechanical contraction. 3DFG MEAs enabled detection of spontaneous FPs from 2D cardiac cultures with high SNR of ca. 27 dB (Fig. 3A). The extracellular FPs present a typical and predominant negative phase and an expected short duration of the Q phase (Na^+ peak) below 30 ms. The spontaneous beating rate of the culture is approximately 60 beats per minute (bpm), as expected for hiPSC-CMs (*34*). As already observed in previous studies using NT-3DFG (*35*), intracellular AP recordings with 3DFG electrodes do not occur in physiological conditions, i.e., without any external stimulation for porating the cellular membrane. This suggests that 3DFG is not spontaneously internalized by the cardiomyocytes despite the tight adhesion formed between the cells and the material.

Stimulation with the 1064-nm ultrafast pulsed laser at ca. 1 mW led to the acquisition of intracellular APs, suggesting successful optoporation of cellular membrane by 3DFG upon illumination with laser pulses. The acquired signals after laser stimulation display a monophasic positive peak and an average duration of 206 ± 28 ms at 50% amplitude calculated over 562 APs measured across the 3DFG MEAs (Fig. 3B). The acquired signals present the expected components of the cardiac APs, i.e., an initial steep depolarization

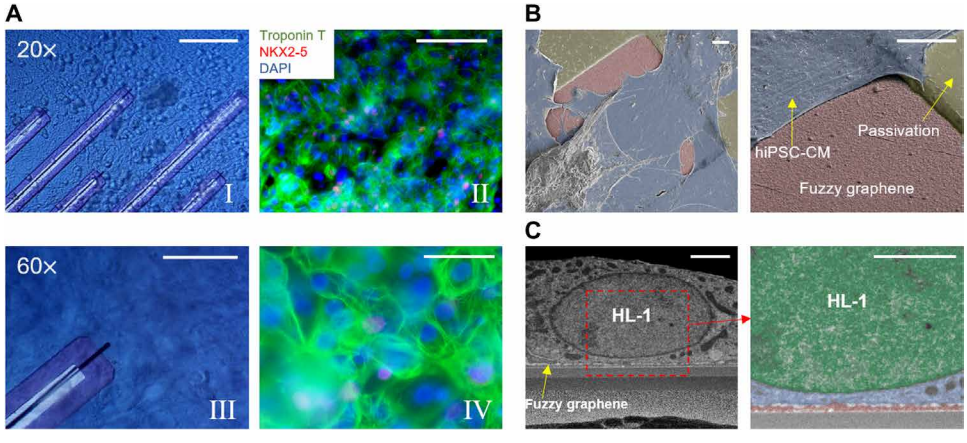

Fig. 2. 3DFG MEA–cardiomyocyte interface. (**A**) Bright-field (I and III) and immunofluorescence images (II and IV) of hiPSC-CMs cultured on 3DFG-MEAs for 7 days in vitro. Scale bars, 100 μm (I and II) and 50 μm (II and IV). (**B**) False-colored SEM images of hiPSC-CMs on 3DFG MEAs. Scale bars, 5 μm. (**C**) Cross-sectional SEM images of HL-1 cells on 3DFG. The right image shows the cell nucleus in green, the cytoplasm in blue, and 3DFG in red. Scale bars, 2 μm.

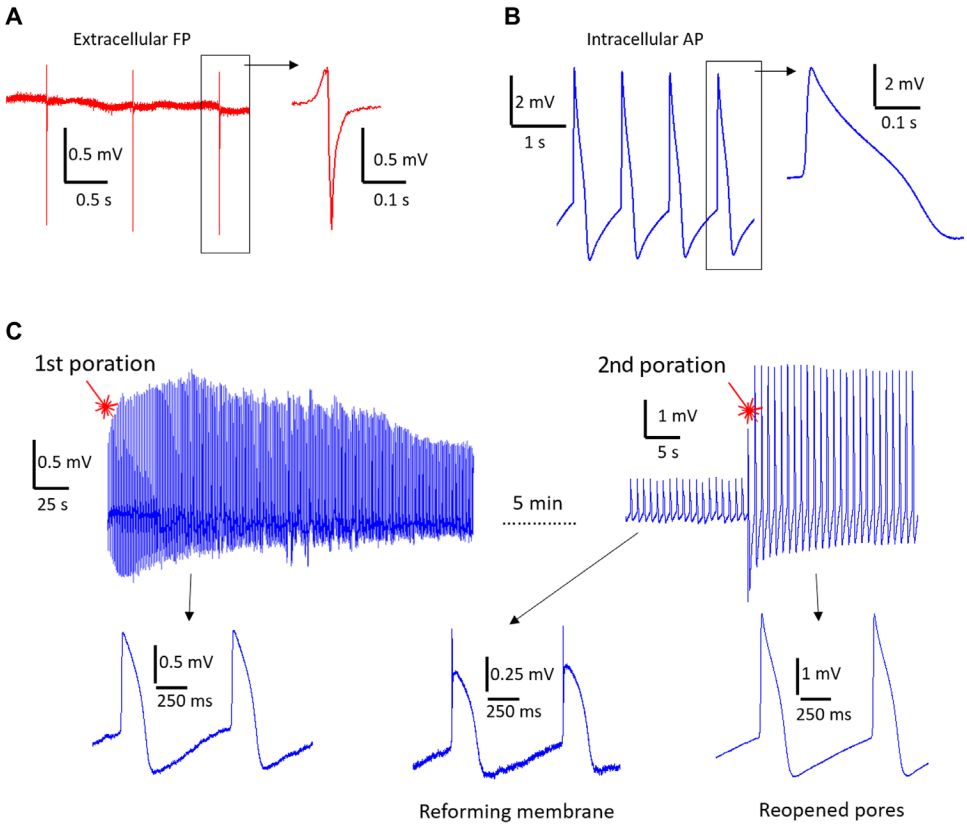

Fig. 3. Electrophysiological recordings. (**A**) Representative extracellular FP recording of hiPSC-CMs using 3DFG-MEA with 50-μm electrodes ($n = 80$ electrodes). (**B**) Representative intracellular AP recording on 3DFG-MEA with 50-μm electrodes after optoporation ($n = 70$ electrodes). (**C**) Time stability of the intracellular coupling after optoporation with the cellular membrane reforming and the extracellular FP reappearing in the signal. On the right, the cardiomyocyte is excited a second time with laser, which produces new pores and recovers the intracellular AP recording.

phase, a slight repolarization followed by a longer plateau, and the final repolarization phase. Cell membrane optoporation may be attributed to the emission of hot carriers from the 3DFG electrode during ultrafast pulsed laser irradiation. As previously reported by several groups (*36*–*38*), the hot carriers, being out of thermal equilibrium, are highly energetic and can form an electron plasma at the interface with 3DFG (*36*–*38*). If the local density of hot carriers is above a certain threshold, the electron plasma relaxation and its collisions with water molecules lead to the generation of cavitation nanobubbles that locally disrupt the cellular membrane. The collisions of the hot electrons with water molecules make their mean free path confined within tens of nanometers from the electrolyte-material interface (*28*). The optoporation event is thus extremely localized within the small area of laser excitation (focused spot size of about 2 μm in diameter). Being most of the optical energy used to emit electrons, the overall process does not affect the local temperature (no heating) (*15*, *28*).

We conducted electrophysiological experiments with cell poration on six 3DFG MEAs distributed in three distinct hiPSC-CM culture preparations (including the experiments in the next section). The success rate of achieving localized optoporation by 3DFG was as high as 90%, in line with previous results obtained with other materials (*15*, *33*). Intracellular APs acquired on 3DFG MEAs showed amplitudes from few hundred microvolts up to 5 to 6 mV (average intracellular AP was ca. 3.56 ± 1.96 mV) and SNR as high as 43 dB. The maximum obtainable amplitude after poration was limited by the specifications of the acquisition system in our experiments (see Materials and Methods). Intracellular APs with amplitude higher than 6 mV were potentially recorded, but the saturation of the amplifiers distorted these signals, which were thus discarded. On average, the 5-μm 3DFG ultramicroelectrodes led to acquisition of APs with higher amplitudes compared to 50-μm microelectrodes. This can be attributed to the small size of the electrodes that leads to higher seal resistance after optoporation (*33*).

To highlight the advantage of multichannel intracellular recordings with 3DFG-MEAs, we report in fig. S6 an example of simultaneous intracellular recordings from several 3DFG electrodes on the same MEA. We obtained these measurements by moving the MEA device under the laser beam and by subsequently applying optoporation on multiple electrodes on the same sample (fig. S5). Because all optoporation events can be completed in few seconds, whereas the intracellular signals are stable for few minutes, we have a comfortable time window for recording intracellular APs simultaneously from several 3DFG electrodes. For cardiomyocytes, these multisite measurements are useful for mapping signal propagation in syncytia in terms of patterns and velocity and for improving data reliability by increasing the number of analyzed cells (*34*). Figure S6 also provides insights on the variability of the acquired intracellular signals. We can observe that the signals present different amplitudes based on the level of intracellular coupling reached after optoporation.

However, the shape of the signals and their duration remain reasonably constant among the cells, with variations that fall within the typical cardiac-type variability of commercial hiPSC-CM lines (*15*).

As observed with other microelectrode materials (*15*), the optoporation process on 3DFG is noninvasive as it can be repeated multiple times on the same cells (Fig. 3C). In the example reported in Fig. 3C, intracellular APs with amplitude of approximately 1.5 mV are recorded for few minutes after the first optoporation event. As the cellular membrane reforms, the signal amplitude decreases and the shape of the extracellular FP starts to be again noticeable. At this point, we reexcite the cell in the close proximity (few micrometers from the first excitation) to enable immediate recovery of the fully intracellular AP shape. The amplitude of the signals after the second poration is higher and reaches approximately 3 mV. However, the duration of the APs does not vary between the first and second poration event [for the case depicted in Fig. 3C, the AP duration (APD50) is 183 ± 23 ms (n = 30 APs) and 176 ± 8 ms (n = 30 APs) after the first and second poration, respectively]. In addition, the beating rate of the culture remains unaltered during the first and second poration events as well. On average, the APs recorded after multiple optoporation events presented higher amplitude because of the increased intracellular coupling area with respect to the total cell-electrode adhesion surface (*4*). In perspective, longer sequences of recordings of intracellular APs may also be achieved by prolonging the intracellular coupling of 3DFG after a single optoporation event. Toward this goal, various strategies from literature could be implemented in future configurations of 3DFG MEAs. Protruding nanostructures to be used as template for 3DFG growth could favor the intracellular coupling by promoting cellular engulfment (*39*) and by inducing the curvature of the cellular membrane, which, in turn, can activate the local recruitment of endocytosis proteins (*40*). For a better evaluation of the intracellular recording performance of 3DFG combined with optoporation, we report in table S1 the main characteristics of our technique together with those of other approaches tested with cardiomyocytes.

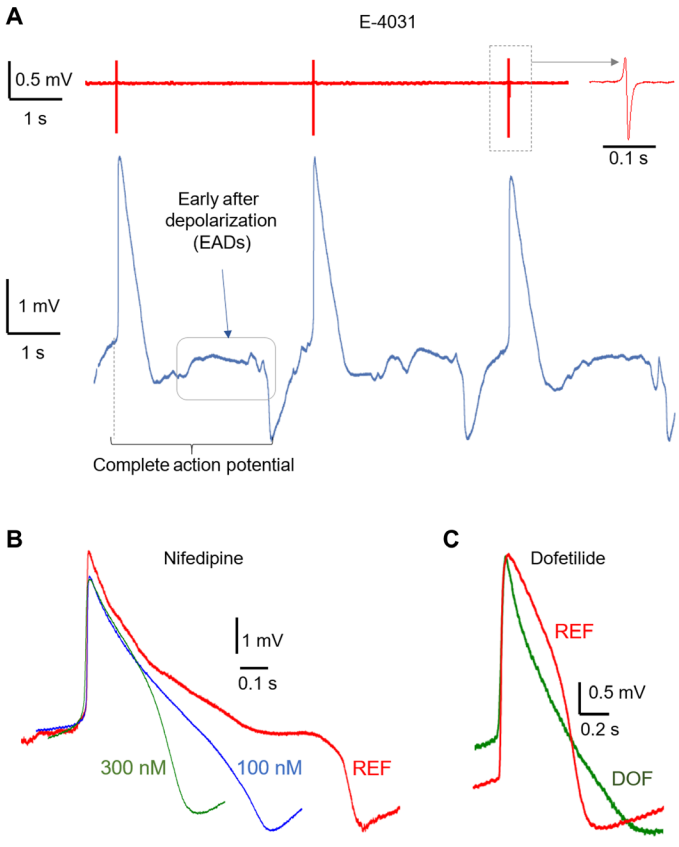

Fig. 4. Compound effects on cardiomyocytes. (**A**) Representative cardiac FPs (red trace) and APs (blue trace) after administration of 2 μM E-4031. The AP trace shows the presence of EADs after the main repolarization phase of the APs. (**B**) Representative cardiac APs before and after administration of nifedipine at various concentrations. (**C**) Representative cardiac APs before and after administration of 100 nM dofetilide (DOF). REF, reference signal in physiological conditions.

Drug effect detection on human-derived cardiomyocytes

We characterized cardiac ionic currents with 3DFG-MEAs by administering different drugs to hiPSC-CMs and measuring the effects on the shape of the APs recorded using 3DFG-MEA. For some of these experiments, we used a different cell line, the Pluricyte cells, which present a longer repolarization with a more pronounced plateau phase, resulting in higher APD50 duration on average (*41*). For Pluricyte hiPSC-CMs, the measurements were conducted after 8 days in vitro (DIV) because these cells require a minimum of 7- to 8-day incubation period before expressing regular spontaneous activity (*41*). We investigated the effect of three compounds, E-4031, nifedipine, and dofetilide, which produce three distinct deformation effects on the shape of the human cardiac APs. The molecule E-4031 is a class III antiarrhythmic drug that prolongs the cardiac AP by blocking potassium channels (*42*). Above a certain concentration, E-4031 leads to notable prolongation of the cardiac AP and occurrence of early after depolarizations (EADs), which are strong indicators of increased arrhythmia risk (*42*). In Fig. 4A, we report representative traces of hiPSC-CM (Pluricyte cell line) FPs (top red trace) and APs (bottom blue trace) from two electrodes of the same 3DFG MEA after the administration of 2 μM E-4031. The APs present a very long APD at 90% amplitude (APD90) of 2.95 ± 0.27 s (35 APs across seven electrodes). In particular, the APs show the typical depolarization phase followed by a partial repolarization. However, these phases are followed by a long plateau phase in which we can observe fluctuations of the membrane potential before the final repolarization phase. Therefore, the recorded signals reproduce correctly the expected effects of E-4031 at high concentration on human-derived cardiomyocytes (*42*).

Nifedipine is a calcium channel blocker that shortens the duration of the cardiac APs (*43*). Figure 4B depicts APs of hiPSC-CMs (Pluricyte cell line) in physiological conditions (red trace) and after administration of 100 and 300 nM nifedipine. The three traces show the anticipated marked shortening of the APs due to the faster repolarization phase (Fig. 4B). In detail, the APD90 is reduced from 915 ± 90 ms (90 APs across nine electrodes) to 535 ± 97 ms for 100 nM (70 APs across seven electrodes) and to 332 ± 75 ms (50 APs across five electrodes) for 300 nM nifedipine. We observe a dose-dependent effect of nifedipine, with a shorter AP duration at higher concentration, as expected for this drug (*42*). Dofetilide is a class III antiarrhythmic agent that blocks the rapid component of the cardiac ion channel delayed rectifier current (*44*). As a result, dofetilide prolongs the repolarization phase and thus the total duration of the APs. In Fig. 4C, we report representative traces of hiPSC-CM APs (Cor.4U cell line) before (red trace) and after (green trace) administration of 100 nM dofetilide. The trace after drug administration

presents a longer repolarization phase. In detail, the APD90 increases from 586 ± 67 ms (50 APs across five electrodes) to 741 ± 101 ms (50 APs across five electrodes). Last, by observing the reference traces in Fig. 4B (red traces, physiological conditions), we note that our measurements correctly report the longer APD50 of the Pluricyte cells with respect to the Cor.4U cells used for the experiments in the previous section and for the dofetilide tests (*41*). In particular, the reference trace in Fig. 4B shows a marked plateau during the repolarization phase. The drug assays confirm that our presented MEA platform can be used to detect changes in electrophysiological activity, which is crucial for diagnostics applications and for screening of therapeutic drugs.

In this work, we present 3DFG-based MEA platform that enables recording of intracellular electrical activity from human-derived cardiomyocytes. The AP recordings are enabled by the combination of unique morphological, optical, and electrochemical properties of 3DFG. Optoporation of cellular membranes by 3DFG upon illumination with ultrafast pulsed laser is attributed to hot carrier generation in the material. 3DFG MEAs show optimal performance for measuring ionic currents in cardiomyocyte cultures, providing intracellular APs with high SNR and allowing the accurate detection of drug effects on the cardiac ion channels. The cell poration process on 3DFG shows very low invasiveness because it can be repeated on the same cell without affecting its health or its spontaneous electrical activity. The possibility to use graphene electrodes for intracellular AP recordings paves the way toward the realization of high-performance, all-carbon MEA biosensing devices. These bioelectronics could provide fundamental features such as high mechanical flexibility for in vivo applications, high biocompatibility for long-term experiments, low cost for pharmaceutical screening applications, and absence of noble metals or polluting materials for environmental considerations. Future efforts will include intracellular recording stabilizations via templated growth from wires or tubes (*18*, *45*, *46*) or surface chemical modifications (*26*, *47*).

MATERIALS AND METHODS

Outer contact/interconnect patterning

A (100) Si substrate with a 600-nm wet thermal oxide wafer (*P* type, ≤0.005 ohm·cm, Nova Electronic Materials Ltd., catalog no. CP02 11208-OX) was cleaned with acetone and isopropyl alcohol (IPA) via sonication for 5 min. The Si/SiO_2 substrate was treated with O_2 plasma, and Pt contacts and interconnects were patterned using photolithography technique (*8*). Briefly, 300-nm LOR3A (MicroChem) was spin-coated at 4000 rpm for 40 s followed by baking at 190°C for 5 min. After baking, 500-nm Shipley S1805 (MicroChem) was spin-coated followed by baking at 115°C for 5 min. The resists were patterned by UV exposure (125 mJ/cm^2) using a mask aligner (Karl Suss MA6) followed by development for 1 min in CD26 developer (MicroChem). Five nanometers of Cr and 100 nm of Pt were evaporated using e-beam evaporator (Kurt J. Lesker), and the liftoff was performed in Remover PG (MicroChem) at 60°C for 30 min, followed by rinsing with acetone and IPA.

3DFG synthesis

3DFG was synthesized through the PECVD process (*18*). The synthesis process was carried out at 800°C and at a total pressure of 0.5 torr. The sample was placed 4 cm from the edge of the radio frequency (RF) coil and out of the PECVD furnace. The temperature of the furnace was ramped up to 800°C in 15 min, followed by a temperature stabilization step at the synthesis temperature for 5 min under a flow of 100 sccm (standard cubic centimeter per minute) Ar (Matheson Gas). Before the synthesis step, inductively coupled plasma was generated using a 13.56-MHz RF power supply (AG 0313 Generator and AIT-600 RF, power supply and auto tuner, respectively, T&C Power Conversion Inc.) with the plasma power constant at 50 W, and the furnace was moved over the sample after plasma ignition. The synthesis step was conducted under 50 sccm CH_4 precursor (5% CH_4 in Ar, Airgas) for 10, 30, or 90 min. The plasma was turned off after the synthesis step, and the sample was rapidly cooled from growth temperature to 100°C under the flow of 100 sccm Ar.

3DFG microelectrode patterning

The patterning of 3DFG microelectrodes was obtained by following the methods previously described in (*35*). After the synthesis, 100-nm SiO_2 film was deposited on the chips using PECVD (Trion Orion) at 375°C, 60 W of power, and 900 mtorr of pressure under 75 sccm of SiH_4 and 70 sccm of N_2O. The SiO_2-coated samples were baked at 95°C for 5 min followed by an O_2 plasma treatment for 1 min at 100 W. A 100-nm Cr hard mask was photolithographically patterned in the shape of the 50-, 10-, and 5-μm electrodes on the SiO_2 layer. SiO_2 from the unpatterned regions was etched off by reactive ion etching (RIE) (Plasma Therm 790 RIE) using 22.5 sccm of CHF_3 and 16 sccm of O_2 at 100 W of power and 100 mtorr of pressure for 5 min. After SiO_2 etching, 3DFG from the nonelectrode regions was also etched off by RIE using 16 sccm of O_2 and 6 sccm of Ar at 20 W of power and 10 mtorr of pressure for 60 min. After etching, Cr hard mask and the underlying SiO_2 film were etched off using Cr etchant (Transene, 1020AC) and buffered oxide etchant (Transene), respectively. The 3DFG electrodes were treated with 69% HNO_3 acid for 2 hours, followed by three times deionized water rinses. Last, the Pt interconnects and the nonrecording site of the 3DFG electrodes were passivated with 2 μm of SU-8 (MicroChem, SU-8 2002).

Scanning electron microscopy

SEM imaging of 3DFG electrodes was performed using an FEI Quanta 600 field emission gun SEM and FEI Helios NanoLab 650. High-resolution images (2048 × 1768 pixels) were acquired at accelerating voltages of 5 to 20 kV with a working distance of 5 mm. No additional conductive coating was applied to the samples to assist with imaging. SEM imaging of fixed cells was performed using FEI Helios NanoLab 650. After depositing a thin Pt layer (≈1 μm) via the gas injection system, trenches were dug with an ionic current of 9.3 and 0.79 nA to reveal the cell-3DFG interface, and a polishing ionic current of 0.79 nA was used to improve the visualization of the cell. For both trenches and polishing, an ion acceleration of 30 kV was used. Samples were imaged at a 52° tilt angle (3 kV, 0.20 nA), and backscattered electrons were collected through the lens detector (TLD) in immersion mode. Images are presented with inverted colors.

Cells were fixed with a solution of 2.5% glutaraldehyde in Na cacodylate buffer (0.1 M) for 1 hour on ice. An RO–T–O staining protocol (*32*) was completed, and samples were embedded in a thin layer of Spurr resin.

Raman spectroscopy

Raman spectroscopy was performed using NT-MDT NTEGRA Spectra with 532-nm excitation through a 100× objective. Raman spectra were acquired with 0.5 neutral density (ND) filter and an acquisition time

of 30 s. Raman spectra were acquired from 30 points across three independent MEA chips.

UV-vis spectroscopy

3DFG was synthesized on 1.5 cm × 1.5 cm fused silica (University Wafer, catalog no. 1013) substrates following the protocol described above. UV-Vis spectra were acquired using an OL 770 multichannel spectroradiometer (Optronic Laboratories Inc.) with xenon light source and integrating sphere. The absorbance was calculated as

$$\text{Absorbance} = 1 - (\text{Reflectance} + \text{Transmittance})$$

Ellipsometry

Ellipsometry measurements were performed by using a J.A. Woollam VASE ellipsometer. Spectroscopic acquisitions were made on a sample with the same composition and morphology of the 3DFG electrodes but larger size. Ellipsometric angles Ψ and Δ were measured in the wavelength range of 300 to 1700 nm for three angles of incidence (50°, 60°, and 70°) and fitted to obtain the dielectric function of the electrodes. The used fitting model consisted of a 500-μm-thick layer of glass as substrate (SiO_2, Palik optical constants) and a 1.5-μm-thick layer made by two Lorentz oscillators for the 3DFG material. The thickness value for the 3DFG layer corresponds to the average thickness of the synthesized 3DFG material, experimentally measured by cross-sectional SEM imaging. The dielectric function of the 3DFG layer was modeled by a Tauc-Lorentz oscillator and two Gaussian oscillators. Two pole oscillators were added to fully model the dispersion of the real part of the dielectric function. These oscillator functions ensure Kramers-Kronig consistency of the real and imaginary parts of the obtained dielectric function for the 3DFG material. The fitting procedure reproduces very well the experimental data, with very low final mean squared error (MSE = 3.1).

Photocurrent measurements

Photocurrent measurements were performed with an Axion 200B amplifier (Molecular Devices, San Jose, CA). The 3DFG MEA was placed on the stage of a Nikon Eclipse FN-1 upright microscope for focusing the picosecond-pulsed laser on the electrodes. The culture well of the 3DFG MEA was filled with PBS, and a platinum wire was immersed in PBS as reference electrode for current measurements. The amplifier headstage was connected to the 3DFG electrode, and voltage-clamp ($V = 0$) traces were acquired during laser illumination.

Electrochemical characterization

Following procedures previously described in (*35*), cyclic voltammetry (CV) and electrochemical impedance spectroscopy (EIS) experiments were conducted using a potentiostat (Metrohm Autolab) in a three-electrode cell setup. To interface the microelectrodes with electrolyte, a polystyrene well was sealed to the MEA chip using 10:1 base:curing agent polydimethylsiloxane (Sylgard 184 Silicone Elastomer, Dow Corning). Pt wire and Ag/AgCl electrodes were used as counter and reference electrodes, respectively. PBS (1×) (Thermo Fisher Scientific, catalog no. 10010023) was used as the electrolyte solution. CV was conducted within a potential range from −1 to 1 V versus Ag/AgCl at a scan rate of 500 mV/s. The current values were normalized to the geometric surface area of the microelectrode. The cathodic charge storage capacity was calculated from the time integral of the cathodic current in the CV curve over a potential range that is just within the water electrolysis window. EIS was performed in the frequency range of 0.1 to 100,000 Hz with V_{DC} of 0 V and V_{AC} of 10 mV. Both CV and EIS experiments were performed inside a grounded Faraday cage. The data were analyzed for $n = 7$ to 8 electrodes for each geometric size and are represented as means ± SD.

Sample preparation for biocompatibility assays

3DFG and Si/SiO_2 control substrates (1 cm × 1 cm) were placed in a 24-well plate and sterilized with 70% ethanol treatment for 1 hour followed by 2-hour UV exposure in the culture hood. After sterilization, the chips were rinsed three times with 1× PBS, followed by 300 μL of fibronectin (50 μg/mL) treatment for 3 hours at room temperature. After incubation, the excess fibronectin was pipetted out followed by three times 1× PBS wash. hESC-CMs were then seeded at a density of 400,000 cells/cm^2 in a 1-mL CDM3 medium supplemented with 10% fetal bovine serum and 2 μM thiazovivin. The samples were incubated at 37°C and 5% CO_2 for 10 days, with CDM3 medium changed every other day. After 6 days in vitro, cell viability and cell stress were investigated (*5*, *8*).

Cell viability

Cell viability was tested by following protocols previously described in (*35*). We used Live/Dead assay kit (Thermo Fisher Scientific, catalog no. L3224) containing calcein acetoxymethyl (calcein AM) and ethidium homodimer dyes for staining live and dead cells, respectively. Nuclei were labeled using Hoechst 33342 dye (Thermo Fisher Scientific, catalog no. 62249). Hoechst, calcein AM, and ethidium homodimer dyes were added with a final concentration of 1 μg/mL, 2 μM, and 4 μM, respectively, to each sample and incubated for 30 min at 37°C and 5% CO_2. Cells were then treated with 10 μM blebbistatin (Sigma-Aldrich, catalog no. B0560) to decouple excitation and contraction, leading to inhibition of spontaneous cell beating (*48*). The cells were washed three times with 1× PBS, and the live-cell imaging was performed at 37°C using an upright confocal microscope (Nikon A1R) under 20×/0.50 numerical aperture (NA) water immersion objective lens. Quantification was performed across four replicates (for both test and control samples) and five images per sample. % Viability was calculated as

$$\%\text{Viability} = \frac{\text{Number of live cells}}{\text{Total number of cells}} \times 100$$

Cell stress

Cell stress was tested using Tetramethylrhodamine, ethyl ester (TMRE) assay kit (Thermo Fisher Scientific, catalog no. T669). TMRE dye is a cell-permeant, cationic, red-orange fluorescent dye that is readily sequestered by active mitochondria. Hoechst and TMRE dyes were added with a final concentration of 1 μg/mL and 50 nM, respectively, to each sample and incubated for 20 min at 37°C and 5% CO_2. The cells were washed three times with 1× PBS, and the live-cell imaging was performed at 37°C using upright confocal microscope under 40×/0.80 NA water immersion objective lens. The fluorescence intensity was quantified from the single channel (red) fluorescent images of 50 to 60 cells across four replicates (for both test and control samples). Data are represented as means ± SD. Statistical analysis was performed using Student's *t* test (two-tailed) (*35*).

Laser-induced cell poration

The cell optoporation setup comprised an upright microscope (Nikon Eclipse FN-1) and a 1064-nm laser pulsed at 8 ps with 12.5-nm repetition period [Nd:YAG (neodymium:yttrium-aluminum-garnet), Plecter Duo, Coherent]. During the experiments, the MEA

acquisition system was placed on the stage of the microscope so that the laser could be focused on the 3DFG electrodes by means of a 60× water immersion objective (NA = 1). A LabVIEW program handled both the acquisition of the electrophysiological signals and the laser stimulation [by controlling with a transistor-transistor logic (TTL) signal a mechanical shutter placed on the optical path of the laser].

Cultures of hiPSC-CMs

hiPSC-derived cardiomyocytes, Cor.4U, and Pluricyte cells were purchased from Ncardia (The Netherlands). Cor.4U cardiomyocytes represent a mixture of ventricular, atrial, and nodal cells, whereas Pluricyte cells are ventricular cardiomyocytes. Cor.4U cells were precultured in T25 culture flasks coated with 1:100 fibronectin in Dulbecco's phosphate buffered saline (DPBS) to remove dead cells and obtain better assay performance. Thereafter, Cor.4U cells were detached using Accumax solution and seeded on the 3DFG-MEAs coated with Geltrex ready-to-use solution (Thermo Fisher Scientific) for 30 min at 37°C, 5% CO_2 in a humidified incubator. Pluricyte cells were plated directly on 3DFG-MEAs coated with fibronectin (Sigma-Aldrich) for 3 hours at 37°C, 5% CO_2 in a humidified incubator. 3DFG-MEAs were previously sterilized by UV exposure for 30 min. Both cell lines were seeded at a density of 30,000 cells per MEA. Electrophysiological recordings were performed 5 to 8 days after plating for Cor.4U cells and 8 to 12 days after plating for Pluricyte cells as suggested by the suppliers.

Immunostaining of hiPSC-CMs

Immunostaining for cardiac troponin T (TNNT2/cTNT) and NKX2-5 was performed on day 7 after plating the hiPSC-CMs on 3DFG-MEAs by using the Human Cardiomyocyte Immunocytochemistry Kit (Life Technologies, A25973). Troponin T is a marker for cardiomyocytes, and NKX2-5 is a marker for early cardiac mesoderm. Cells were fixed with 4% (w/v) formaldehyde in DPBS for 15 min and incubated with the permeabilization solution (1% saponin in DPBS) for 15 min. Thereafter, blocking was performed using 3% bovine serum albumin for 30 min followed by incubation with primary antibodies, NKX2-5 (rabbit anti-NKX2-5 A25974) and TNNT2 (mouse anti-TNNT2 A25969), diluted 1:1000 in the blocking solution for 3 hours at room temperature. After washing three times with wash buffer, the cells were incubated for 1 hour at room temperature with secondary antibodies (Alexa Fluor 488 donkey anti-mouse and Alexa Fluor 555 donkey anti-rabbit) diluted 1:250 in blocking solution. Last, cells were counterstained with 4′,6-diamidino-2-phenylindole (DAPI) and imaged on an upright microscope (Nikon Eclipse FN1) with an air 20× objective or a water immersion 60× objective.

Electrophysiological recordings

The electrophysiological signals were acquired with a custom-made MEA acquisition system based on the amplifier chip RHA2032 from Intan Technologies (Los Angeles, CA). The system provides 24 acquisition channels acquired at 10-kHz sampling rate, 200 gain, and ±5-mV range. Further details of the system can be found in a previous work (*4*). The SNR was calculated as $20 \times \log_{10}(\text{Signal (V)}/\text{Noise (V)})$, with the noise calculated as 6.6 times the root mean square of the trace without the signal.

SUPPLEMENTARY MATERIALS

Supplementary material for this article is available at http://advances.sciencemag.org/cgi/content/full/7/15/eabd5175/DC1

REFERENCES AND NOTES

1. J. Müller, M. Ballini, P. Livi, Y. Chen, M. Radivojevic, A. Shadmani, V. Viswam, I. L. Jones, M. Fiscella, R. Diggelmann, A. Stettler, U. Frey, D. J. Bakkum, A. Hierlemann, High-resolution CMOS MEA platform to study neurons at subcellular, cellular, and network levels. *Lab Chip* **15**, 2767–2780 (2015).
2. J. Abbott, T. Ye, L. Qin, M. Jorgolli, R. S. Gertner, D. Ham, H. Park, CMOS nanoelectrode array for all-electrical intracellular electrophysiological imaging. *Nat. Nanotechnol.* **12**, 460–466 (2017).
3. Y. Zhao, S. S. You, A. Zhang, J.-H. Lee, J. Huang, C. M. Lieber, Scalable ultrasmall three-dimensional nanowire transistor probes for intracellular recording. *Nat. Nanotechnol.* **14**, 783–790 (2019).
4. M. Dipalo, H. Amin, L. Lovato, F. Moia, V. Caprettini, G. C. Messina, F. Tantussi, L. Berdondini, F. De Angelis, Intracellular and extracellular recording of spontaneous action potentials in mammalian neurons and cardiac cells with 3D plasmonic nanoelectrodes. *Nano Lett.* **17**, 3932–3939 (2017).
5. S. K. Rastogi, G. Raghavan, G. Yang, T. Cohen-Karni, Effect of graphene on nonneuronal and neuronal cell viability and stress. *Nano Lett.* **17**, 3297–3301 (2017).
6. K. I. Bolotin, K. J. Sikes, Z. Jiang, M. Klima, G. Fudenberg, J. Hone, P. Kim, H. L. Stormer, Ultrahigh electron mobility in suspended graphene. *Solid State Commun.* **146**, 351–355 (2008).
7. U. Stöberl, U. Wurstbauer, W. Wegscheider, D. Weiss, J. Eroms, Morphology and flexibility of graphene and few-layer graphene on various substrates. *Appl. Phys. Lett.* **93**, 051906 (2008).
8. S. K. Rastogi, J. Bliley, D. J. Shiwarski, G. Raghavan, A. W. Feinberg, T. Cohen-Karni, Graphene microelectrode arrays for electrical and optical measurements of human stem cell-derived cardiomyocytes. *Cell. Mol. Bioeng.* **11**, 407–418 (2018).
9. L. H. Hess, M. Jansen, V. Maybeck, M. V. Hauf, M. Seifert, M. Stutzmann, I. D. Sharp, A. Offenhäusser, J. A. Garrido, Graphene transistor arrays for recording action potentials from electrogenic cells. *Adv. Mater.* **23**, 5045–5049 (2011).
10. T. Cohen-Karni, Q. Qing, Q. Li, Y. Fang, C. M. Lieber, Graphene and nanowire transistors for cellular interfaces and electrical recording. *Nano Lett.* **10**, 1098–1102 (2010).
11. D.-W. Park, A. A. Schendel, S. Mikael, S. K. Brodnick, T. J. Richner, J. P. Ness, M. R. Hayat, F. Atry, S. T. Frye, R. Pashaie, S. Thongpang, Z. Ma, J. C. Williams, Graphene-based carbon-layered electrode array technology for neural imaging and optogenetic applications. *Nat. Commun.* **5**, 5258 (2014).
12. B. Sakmann, E. Neher, Patch clamp techniques for studying ionic channels in excitable membranes. *Annu. Rev. Physiol.* **46**, 455–472 (1984).
13. H. B. Hayes, A. M. Nicolini, C. A. Arrowood, S. A. Chvatal, D. W. Wolfson, H. C. Cho, D. D. Sullivan, J. Chal, B. Fermini, M. Clements, J. D. Ross, D. C. Millard, Novel method for action potential measurements from intact cardiac monolayers with multiwell microelectrode array technology. *Sci. Rep.* **9**, 11893 (2019).
14. J. Abbott, T. Ye, K. Krenek, R. S. Gertner, S. Ban, Y. Kim, L. Qin, W. Wu, H. Park, D. Ham, A nanoelectrode array for obtaining intracellular recordings from thousands of connected neurons. *Nat. Biomed. Eng.* **4**, 232–241 (2019).
15. M. Dipalo, G. Melle, L. Lovato, A. Jacassi, F. Santoro, V. Caprettini, A. Schirato, A. Alabastri, D. Garoli, G. Bruno, F. Tantussi, F. De Angelis, Plasmonic meta-electrodes allow intracellular recordings at network level on high-density CMOS-multi-electrode arrays. *Nat. Nanotechnol.* **13**, 965–971 (2018).
16. K. J. Tielrooij, J. C. W. Song, S. A. Jensen, A. Centeno, A. Pesquera, A. Zurutuza Elorza, M. Bonn, L. S. Levitov, F. H. L. Koppens, Photoexcitation cascade and multiple hot-carrier generation in graphene. *Nat. Phys.* **9**, 248–252 (2013).
17. Y. Lu, B. Ma, Y. Yang, E. Huang, Z. Ge, T. Zhang, S. Zhang, L. Li, N. Guan, Y. Ma, Y. Chen, High activity of hot electrons from bulk 3D graphene materials for efficient photocatalytic hydrogen production. *Nano Res.* **10**, 1662–1672 (2017).
18. R. Garg, S. K. Rastogi, M. Lamparski, S. C. de la Barrera, G. T. Pace, N. T. Nuhfer, B. M. Hunt, V. Meunier, T. Cohen-Karni, Nanowire-mesh-templated growth of out-of-plane three-dimensional fuzzy graphene. *ACS Nano* **11**, 6301–6311 (2017).
19. A. N. Yaroslavsky, P. C. Schulze, I. V. Yaroslavsky, R. Schober, F. Ulrich, H.-J. Schwarzmaier, Optical properties of selected native and coagulated human brain tissues in vitro in the visible and near infrared spectral range. *Phys. Med. Biol.* **47**, 2059–2073 (2002).
20. X. Li, Z. Lv, H. Zhu, Carbon/silicon heterojunction solar cells: State of the art and prospects. *Adv. Mater.* **27**, 6549–6574 (2015).
21. H. Lin, B. C. P. Sturmberg, K.-T. Lin, Y. Yang, X. Zheng, T. K. Chong, C. M. de Sterke, B. Jia, A 90-nm-thick graphene metamaterial for strong and extremely broadband absorption of unpolarized light. *Nat. Photonics* **13**, 270–276 (2019).
22. K. Mizuno, J. Ishii, H. Kishida, Y. Hayamizu, S. Yasuda, D. N. Futaba, M. Yumura, K. Hata, A black body absorber from vertically aligned single-walled carbon nanotubes. *Proc. Natl. Acad. Sci. U.S.A.* **106**, 6044–6047 (2009).
23. S. Zeng, D. Baillargeat, H.-P. Ho, K.-T. Yong, Nanomaterials enhanced surface plasmon resonance for biological and chemical sensing applications. *Chem. Soc. Rev.* **43**, 3426–3452 (2014).

24. Y. Jiang, R. Parameswaran, X. Li, J. L. Carvalho-de-Souza, X. Gao, L. Meng, F. Bezanilla, G. M. G. Shepherd, B. Tian, Nongenetic optical neuromodulation with silicon-based materials. *Nat. Protoc.* **14**, 1339–1376 (2019).
25. T. Zhang, H. Chang, Y. Wu, P. Xiao, N. Yi, Y. Lu, Y. Ma, Y. Huang, K. Zhao, X.-Q. Yan, Z.-B. Liu, J.-G. Tian, Y. Chen, Macroscopic and direct light propulsion of bulk graphene material. *Nat. Photonics* **9**, 471–476 (2015).
26. S. K. Rastogi, R. Garg, M. G. Scopelliti, B. I. Pinto, J. E. Hartung, S. Kim, C. G. E. Murphey, N. Johnson, D. S. Roman, F. Bezanilla, J. F. Cahoon, M. S. Gold, M. Chamanzar, T. Cohen-Karni, Remote nongenetic optical modulation of neuronal activity using fuzzy graphene. *Proc. Natl. Acad. Sci. U.S.A.* **117**, 13339–13349 (2020).
27. J. L. Carvalho-de-Souza, B. I. Pinto, D. R. Pepperberg, F. Bezanilla, Optocapacitive generation of action potentials by microsecond laser pulses of nanojoule energy. *Biophys. J.* **114**, 283–288 (2018).
28. P. Zilio, M. Dipalo, F. Tantussi, G. C. Messina, F. De Angelis, Hot electrons in water: Injection and ponderomotive acceleration by means of plasmonic nanoelectrodes. *Light Sci. Appl.* **6**, e17002 (2017).
29. I. Opris, M. A. Lebedev, V. M. Pulgar, R. Vidu, M. Enachescu, M. F. Casanova, Editorial: Nanotechnologies in neuroscience and neuroengineering. *Front. Neurosci.* **14**, 33 (2020).
30. M. Adamcova, V. Skarkova, J. Seifertova, E. Rudolf, Cardiac troponins are among targets of doxorubicin-induced cardiotoxicity in hiPCS-CMs. *Int. J. Mol. Sci.* **20**, 2638 (2019).
31. V. George, S. Colombo, K. L. Targoff, An early requirement for *nkx*2.5 ensures the first and second heart field ventricular identity and cardiac function into adulthood. *Dev. Biol.* **400**, 10–22 (2015).
32. F. Santoro, W. Zhao, L.-M. Joubert, L. Duan, J. Schnitker, Y. van de Burgt, H.-Y. Lou, B. Liu, A. Salleo, L. Cui, Y. Cui, B. Cui, Revealing the cell–material interface with nanometer resolution by focused ion beam/scanning electron microscopy. *ACS Nano* **11**, 8320–8328 (2017).
33. G. Melle, G. Bruno, N. Maccaferri, G. Iachetta, N. Colistra, A. Barbaglia, M. Dipalo, F. De Angelis, Intracellular recording of human cardiac action potentials on market-available multielectrode array platforms. *Front. Bioeng. Biotechnol.* **8**, 66 (2020).
34. K. Blinova, Q. Dang, D. Millard, G. Smith, J. Pierson, L. Guo, M. Brock, H. R. Lu, U. Kraushaar, H. Zeng, H. Shi, X. Zhang, K. Sawada, T. Osada, Y. Kanda, Y. Sekino, L. Pang, T. K. Feaster, R. Kettenhofen, N. Stockbridge, D. G. Strauss, G. Gintant, International multisite study of human-induced pluripotent stem cell-derived cardiomyocytes for drug proarrhythmic potential assessment. *Cell Rep.* **24**, 3582–3592 (2018).
35. S. K. Rastogi, J. Bliley, L. Matino, R. Garg, F. Santoro, A. W. Feinberg, T. Cohen-Karni, Three-dimensional fuzzy graphene ultra-microelectrodes for subcellular electrical recordings. *Nano Res.* **13**, 1444–1452 (2020).
36. M. Schomaker, J. Baumgart, D. Motekaitis, D. Heinemann, J. Krawinkel, M. Pangalos, W. Bintig, E. Boulais, R. Lachaine, B. St.-Louis Lalonde, A. Ngezahayo, M. Meunier, A. Heisterkamp, in *Frontiers in Ultrafast Optics: Biomedical, Scientific, and Industrial Applications XI* (SPIE Proceedings, 2011), vol. 7925.
37. A. Ben-Yakar, D. Eversole, O. Ekici, in *Nanotechnologies for the Life Sciences* (Wiley, 2010).
38. É. Boulais, R. Lachaine, M. Meunier, Plasma mediated off-resonance plasmonic enhanced ultrafast laser-induced nanocavitation. *Nano Lett.* **12**, 4763–4769 (2012).
39. M. E. Spira, A. Hai, Multi-electrode array technologies for neuroscience and cardiology. *Nat. Nanotechnol.* **8**, 83–94 (2013).
40. H. Y. Lou, W. Zhao, X. Li, L. Duan, A. Powers, M. Akamatsu, F. Santoro, A. F. McGuire, Y. Cui, D. G. Drubin, B. Cui, Membrane curvature underlies actin reorganization in response to nanoscale surface topography. *Proc. Natl. Acad. Sci. U.S.A.* **116**, 23143–23151 (2019).
41. A. Obergrussberger, K. Juhasz, U. Thomas, S. Stölzle-Feix, N. Becker, L. Dörr, M. Beckler, C. Bot, M. George, N. Fertig, Safety pharmacology studies using EFP and impedance. *J. Pharmacol. Toxicol. Methods* **81**, 223–232 (2016).
42. K. S. Lee, T. D. Tsai, E. W. Lee, Membrane activity of class III antiarrhythmic compounds; a comparison between ibutilide, d-sotalol, E-4031, sematilide and dofetilide. *Eur. J. Pharmacol.* **234**, 43–53 (1993).
43. K. Harris, M. Aylott, Y. Cui, J. B. Louttit, N. C. McMahon, A. Sridhar, Comparison of electrophysiological data from human-induced pluripotent stem cell-derived cardiomyocytes to functional preclinical safety assays. *Toxicol. Sci.* **134**, 412–426 (2013).
44. H. Roukoz, W. Saliba, Dofetilide: A new class III antiarrhythmic agent. *Expert Rev. Cardiovasc. Ther.* **5**, 9–19 (2007).
45. Z. C. Lin, C. Xie, Y. Osakada, Y. Cui, B. Cui, Iridium oxide nanotube electrodes for sensitive and prolonged intracellular measurement of action potentials. *Nat. Commun.* **5**, 3206 (2014).
46. L. Matino, S. K. Rastogi, L. D. Garma, T. Cohen-Karni, F. Santoro, Characterization of the coupling between out-of-plane graphene and electrogenic cells. *Adv. Mater. Interfaces* **7**, 2000699 (2020).
47. A. Hai, J. Shappir, M. E. Spira, In-cell recordings by extracellular microelectrodes. *Nat. Methods* **7**, 200–202 (2010).
48. M. Kovács, J. Tóth, C. Hetényi, A. Málnási-Csizmadia, J. R. Sellers, Mechanism of blebbistatin inhibition of myosin II. *J. Biol. Chem.* **279**, 35557–35563 (2004).

Acknowledgments

Funding: T.C.-K. acknowledges funding support from the NSF under award no. CBET1552833, the Office of Naval Research under award no. N000141712368, and the Defense Advanced Research Projects Agency under award no. AWD00001593 (416052-5). S.K.R., R.G., and T.C.-K. also acknowledge support from the Department of Materials Science and Engineering Materials Characterization Facility (MCF-677785). J.B. and A.W.F. acknowledge financial support from the Dowd Fellowship from the College of Engineering at Carnegie Mellon University. **Author contributions:** F.D.A. and T.C.-K. designed the experiment. S.K.R. and R.G. fabricated the 3DFG MEAs and performed sample characterization and biocompatibility experiments. M.D. designed the packaging of the 3DFG MEAs, performed photocurrent measurements, and performed the electrophysiology experiments. G.M. and G.I. performed hiPSC-CM cultures, immunohistochemistry, and electrophysiology experiments. A.B. performed ellipsometry measurements. L.M. and F.S. performed cell fixation and SEM imaging. A.W.F. provided the needed hESC-CM expertise for the toxicity study. J.B. cultured the hESC-CM. R.S. and S.S. helped with the UV-Vis measurements. All authors wrote, read, and approved the manuscript. **Competing interests:** F.D.A. and M.D. are inventors of patent application WO2019116257A1, related to cell optoporation. F.D.A., M.D., and G.I. are shareholders of the Italian company FORESEE Biosystems srl, which works on cell optoporation systems. G.M. is the chief executive officer (CEO) of FORESEE Biosystems srl. T.C.-K., S.K.R., R.G., A.B., L.M., F.S., A.W.F., J.B., R.S., and S.S. declare that they have no competing interests. **Data and materials availability:** All data needed to evaluate the conclusions in the paper are present in the paper and/or the Supplementary Materials. Additional data related to this paper may be requested from the authors.

Submitted 29 June 2020
Accepted 17 February 2021
Published 7 April 2021
10.1126/sciadv.abd5175

Citation: M. Dipalo, S. K. Rastogi, L. Matino, R. Garg, J. Bliley, G. Iachetta, G. Melle, R. Shrestha, S. Shen, F. Santoro, A. W. Feinberg, A. Barbaglia, T. Cohen-Karni, F. De Angelis, Intracellular action potential recordings from cardiomyocytes by ultrafast pulsed laser irradiation of fuzzy graphene microelectrodes. *Sci. Adv.* **7**, eabd5175 (2021).

ScienceAdvances

Intracellular action potential recordings from cardiomyocytes by ultrafast pulsed laser irradiation of fuzzy graphene microelectrodes

Michele DipaloSahil K. RastogiLaura MatinoRaghav GargJacqueline BlileyGiuseppina IachettaGiovanni MelleRamesh ShresthaSheng ShenFrancesca SantoroAdam W. FeinbergAndrea BarbagliaTzahi Cohen-KarniFrancesco De Angelis

Sci. Adv., 7 (15), eabd5175. • DOI: 10.1126/sciadv.abd5175

Science Advances (ISSN 2375-2548) is published by the American Association for the Advancement of Science. 1200 New York Avenue NW, Washington, DC 20005. The title *Science Advances* is a registered trademark of AAAS.